

Multilayer three-dimensional super resolution imaging of thick biological samples

Alipasha Vaziri¹, Jianyong Tang, Hari Shroff, and Charles V. Shank¹

Howard Hughes Medical Institute, Janelia Farm Research Campus, Ashburn, VA 20147

Contributed by Charles V. Shank, October 23, 2008 (sent for review September 30, 2008)

Recent advances in optical microscopy have enabled biological imaging beyond the diffraction limit at nanometer resolution. A general feature of most of the techniques based on photoactivated localization microscopy (PALM) or stochastic optical reconstruction microscopy (STORM) has been the use of thin biological samples in combination with total internal reflection, thus limiting the imaging depth to a fraction of an optical wavelength. However, to study whole cells or organelles that are typically up to 15 μm deep into the cell, the extension of these methods to a three-dimensional (3D) super resolution technique is required. Here, we report an advance in optical microscopy that enables imaging of protein distributions in cells with a lateral localization precision better than 50 nm at multiple imaging planes deep in biological samples. The approach is based on combining the lateral super resolution provided by PALM with two-photon temporal focusing that provides optical sectioning. We have generated super-resolution images over an axial range of $\approx 10 \mu\text{m}$ in both mitochondrially labeled fixed cells, and in the membranes of living *S2 Drosophila* cells.

nanoscopy | PALM microscopy | 3D imaging | temporal focusing

Initial studies, based on defocusing (1), astigmatism (2), and others (3), have extended super resolution imaging (2, 4–13) to three dimensions (3D); however, only up to a few hundred nanometers in depth in biological samples. This is mainly due to the following: In photoactivated localization microscopy (PALM) (6, 12) and stochastic optical reconstruction microscopy (STORM) (8), a sufficient signal-to-noise ratio is required to discriminate single molecules from the background. In the defocusing approaches, background typically increases with imaging depth and the signal is further reduced as it is spread out across more pixels, making the signal to noise ratio insufficient for molecules that are more than a few hundred nanometers away from the focal plane. In addition, PALM is inherently a wide-field technique that is not well suited to point-scanning methods. The reason for this is 2-fold: First, in PALM, single molecules need to be *imaged*, that is, their emission has to be spread out across several pixels (6) and second, data are most efficiently collected when emissions from spatially segregated molecules are recorded in parallel—point-scanning methods are inherently serial, and are thus slower than wide-field methods (14).

Thus, super resolution imaging would benefit greatly by adopting a wide-field technique and combining it with optical sectioning for enhanced signal to noise ratio at depth.

In this article, we describe a method whereby a thin layer of photoactivatable fluorescent proteins (15) can selectively be activated in a location several micrometers deep in a cellular sample. This thin layer is then excited and imaged using the PALM technique with a demonstrated resolution of better than 50 nm. A succession of thin layer images can be combined to produce a volume image several micrometers in depth.

In a two-photon absorption process, the molecular excitation probability is proportional to the square of the intensity of the optical pulses. Thus, for constant pulse energy, the excitation probability in the focal plane can be increased by reducing the pulse width. In this approach, the molecular excitation is in-

versely proportional to pulse width squared and is called temporal focusing (16, 17). Temporal focusing is experimentally achieved by first broadening the pulse using a dispersive optical element such as a grating. The illuminated spot on the grating is then imaged onto the specimen plane using a telescope. This results in a pulse broadened everywhere in the sample except at the image plane, where the dispersion is compensated and the pulse reaches its minimum width (Fig. 1). Compared with an epi-fluorescence technique, this minimum width results in a depth of field that is orders of magnitude smaller (see [supporting information \(SI\) Fig. S1](#) and [SI Materials and Methods](#)). Therefore, temporal focusing can be used for selective excitation of a thin layer of molecules in a biological sample.

The short depth of field of the temporal focusing and the fact that it is a wide-field technique makes it a suitable technique for subsurface layer PALM. Ideally, temporal focusing PALM would employ both two spatially overlapping two-photon, temporally focused beams, one at the two-photon excitation peak and the other at the two-photon activation peak of the photoactivatable protein. In this fashion, the two-photon activation of molecules would prevent all other molecules that are not in the same layer from unnecessary exposure and the two-photon excitation would lead to lower out-of-focus background. Temporal focusing PALM is also possible as long as sufficient overlap between the two-photon absorption spectrum of either the excitation or the activation of the desired photoactivatable fluorescent protein and the temporal focusing laser exists. In this case, the one of the beams can be implemented in a one-photon absorption wide-field configuration.

The localization precision provided by PALM is complemented when photoactivatable fluorescent proteins are used. These can be genetically expressed in a nonperturbative manner with high specificity in a target area that allows for functional cellular studies on the molecular level.

Results and Discussion

Depth of Field in Temporal Focusing. In temporal focusing, the localization of excitation extends over the entire field of view and the intensity in the lateral plane drops off in the axial direction for a typical experimental configuration ≈ 75 times faster (16, 17) ([Fig. S1](#)) than a Gaussian beam with the same waist size. This gives the temporal focusing a depth of field and sectioning capability that is comparable with a confocal or two-photon microscope (18). We experimentally confirmed this by comparing the depth of focus of the temporal focusing in our setup with the depth of focus when the effect of the temporal focusing was removed (see [SI Materials and Methods](#)). The depth of field of the

Author contributions: A.V. and C.V.S. designed research; A.V., J.T., and H.S. performed research; A.V. and J.T. analyzed data; and A.V. wrote the paper.

The authors declare no conflict of interest.

Freely available online through the PNAS open access option.

¹To whom correspondence may be addressed. E-mail: vaziria@janelia.hhmi.org or shank380@yahoo.com.

This article contains supporting information online at www.pnas.org/cgi/content/full/0810636105/DCSupplemental.

© 2008 by The National Academy of Sciences of the USA

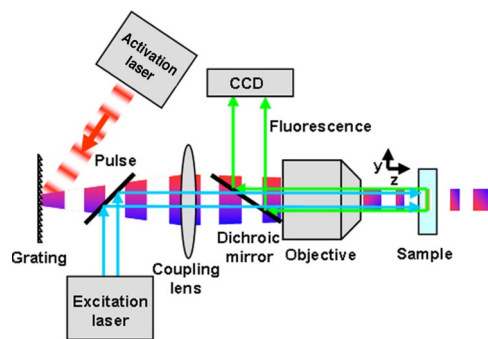


Fig. 1. Experimental setup for temporal focusing PALM. The activation light is provided by a two-photon temporally focused beam and the excitation light by a one-photon laser. Temporal focusing of the propagating pulse is achieved by imaging a spot on a grating onto the specimen via a two lens system (objective plus coupling lens). This 4f imaging configuration ensures that the pulse has the same (shortest) width in the specimen as at the grating, but the spatial and temporal dispersion caused by the grating generates a longer pulse outside the focal region.

temporal focusing given our experimental parameters was measured to be $1.9 \mu\text{m}$.

After confirming the sectioning performance of temporal focusing by axially scanning a thin fluorescent layer across the focal plane (see *SI Materials and Methods*), we next examined various biological samples. Acute transverse hippocampal slices ($400 \mu\text{m}$) from rat were prepared, microinjected with a fluorescent dye, and imaged in $1\text{-}\mu\text{m}$ steps over a range of $100 \mu\text{m}$ (see *Movie S1*). Four of the images at $10\text{-}\mu\text{m}$ intervals are shown in Fig. 2. Individual dendritic spines at different locations are visible in each frame. In acute slices, dendritic spines are typically only visible in a confocal or scanning two-photon microscope and to our

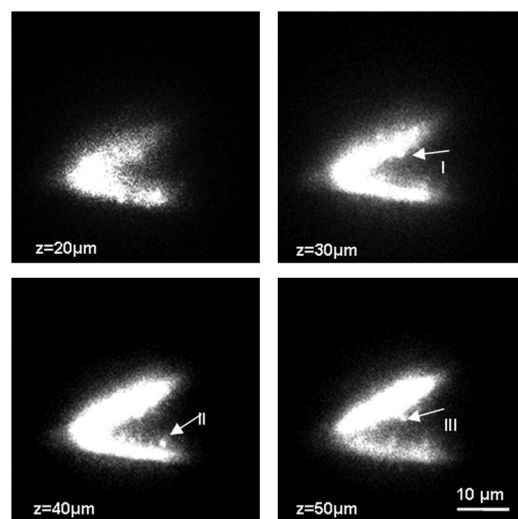


Fig. 2. Visualization of dendritic spines using temporal focusing. The depth of focus for a temporally focused beam with a spot size of $\approx 15 \mu\text{m}$ is shown. It is $\approx 1.9 \mu\text{m}$, which is ≈ 75 times smaller than for the same spot size without temporal focusing (see *SI Materials and Methods*). Individual dendritic spines at different locations of a branched dendrite are visualized using temporal focusing. Top left image shows the membrane boundary of the two dendrites whereas the rest of images show the individual spines at I, II, and III coming in and going out of focus (see *Movie S1* for the animation $>100 \mu\text{m}$). Images were taken at $10\text{-}\mu\text{m}$ steps in an acute hippocampal slice. Because the spines contained a lower concentration of dye compared with dendrites, the laser intensity was increased for the visualization of individual spines, which resulted in the saturation of the image at the dendrites.

knowledge have not been followed in 3D or in depth in a wide-field configuration.

Using Temporal Focusing for Super Resolution in 3D. For temporal focusing PALM experiments, we used a two-photon activation, one-photon excitation approach and determined the suitability of several photoactivatable fluorescent proteins for this scheme. The two-photon activation responses of EosFP (19), Kikume (20), and Dronpa (21) were studied by using temporal focusing. We identified Dronpa as the molecule with the highest response to the temporal focusing activation light and chose it as the photoactivatable fluorescent protein for the following experiments. Under our experimental conditions, we collected an average of ≈ 600 photons from each Dronpa molecule before it switched off or bleached. Using other photoactivatable fluorescent proteins (such as EosFP), which emit more photons before bleaching and have a higher contrast ratio (ratio of the fluorescence intensity between the on and the off state), would likely allow a higher localization precision, lower background, and higher resolution (6). Efforts are underway in our laboratory to exploit these advantages by designing a tunable temporal focusing laser, thus allowing temporal focusing for both activation and excitation of many different photoactivatable fluorescent proteins.

The power for the activation laser was adjusted to activate just one molecule per diffraction limited area per frame within the acquisition time. The activated molecules were excited and imaged via a lens system, designed to fulfill the Nyquist-Shannon criterion (see ref. 22), onto an EMCCD camera until bleached. Subsequently, another subset of the molecules was photoactivated, excited, and bleached. This process was repeated for each layer until all molecules in that layer were bleached. Then, using a piezo element stage, the sample was axially translated by $\approx 1 \mu\text{m}$ and molecules in the next layer were imaged. We typically took PALM images from 5 to 8 different layers over a range of up to $10 \mu\text{m}$ within the cells.

Since in each layer the molecules within a single diffraction-limited volume are imaged at different times, their diffraction-limited emissions do not overlap. The centre of each molecular point spread function can thus be determined to a precision better than the diffraction limit, and assembling the aggregate position information from all molecules results in a super resolution image. The image processing was done using custom PALM analysis software (6). This routine searches for intensity peaks and fits them to 2D Gaussian profiles. As described in ref. 6, the Gaussian fit parameters, number of photons and background counts are used to determine the molecular positions and the corresponding localization uncertainties. The molecules are then rendered as Gaussian peaks with widths equal to these localization uncertainties so that the brightness of each pixel in the rendered PALM image can be interpreted as the probability distribution for finding the molecule at that location. However, in image processing there is a fundamental tradeoff between the number of molecules rendered and the image resolution; including fewer, but brighter, molecules results in higher localization and crisper images but at a reduced molecular density, giving less complete information about the spatial distribution of the target protein. In this article, we rendered all molecules that were localized to within 50 nm ; this condition resulted in $\approx 80\%$ of localized molecules being plotted.

Multilayer PALM of Mitochondrial Matrix and *Drosophila* S2 Cell Membrane. As our first sample, we imaged fixed HFF1-cells that expressed Dronpa in the mitochondrial matrix (Fig. 3A). Mitochondrial expression was achieved by appending the mitochondrial matrix targeting sequence from cytochrome *c* oxidase VIII to the Dronpa fluorescent protein to mediate the import of Dronpa into the mitochondria (see *SI Materials and Methods* for details).

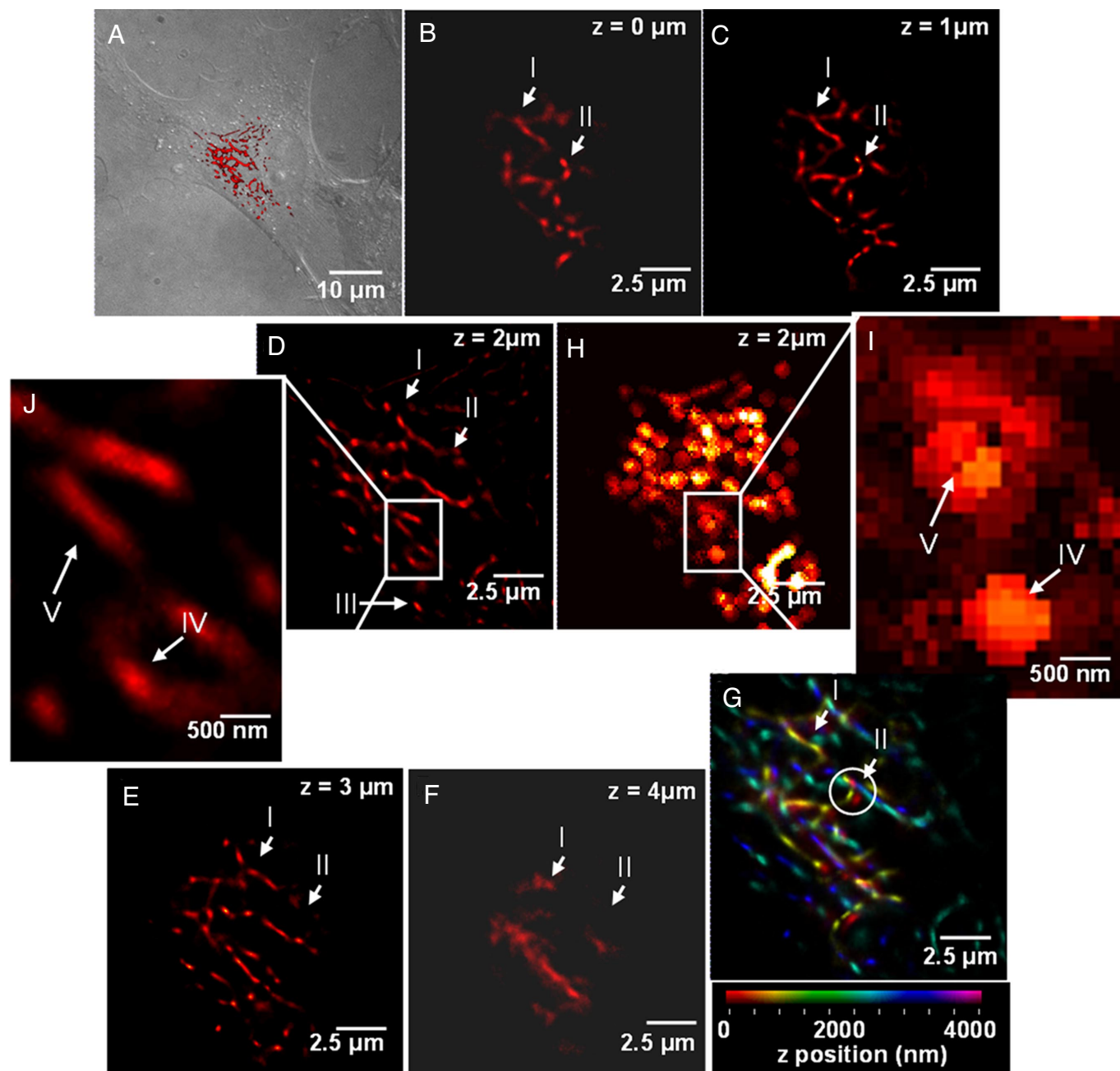


Fig. 3. Multilayer super resolution imaging of mitochondrial network $>5 \mu\text{m}$ in depth. (A) Overview of the region where the images were taken at $4\times$ lower magnification than (B–G). The DIC images of the cell are overlaid with an epifluorescent image taken by a Xenon lamp and subsequently overlaid with (D) (red region). (B–F) PALM images of mitochondrial networks in HFF1-cell labeled with Dronpa taken in $1\text{-}\mu\text{m}$ steps. Different axial regions of the same mitochondria (region marked between I and II in B–E) and individual mitochondria (III in D) can be seen at different focal depths. (D and H) Comparison of the PALM image and the sum of diffraction-limited images for the same layer. (J and I) Five-fold magnification of a selected region from D and H, respectively. Several features seen as individual structures in J (IV and V) are clearly below the resolution limit in at the respective locations in I. (G) Superposition of (B–F) where the axial position is represented using a color map. (G) The 3D topology of the mitochondrial network. Interestingly, there are several features which are laterally as close as $\approx 200 \text{ nm}$ but originate from planes that are axially $3 \mu\text{m}$ apart (structures within the circle in G). The volume information in (G) was further used to create a 3D animation (See [SI Movie S2](#)).

Fig. 3 B–F shows a series of these images taken in $1\text{-}\mu\text{m}$ steps from Dronpa-labeled reticular mitochondrial networks. Each PALM image contains structural details about the location of individual molecules and their relative locations, information that is not evident in the matching diffraction-limited images (Fig. 3 H and I). Moreover, the fact that images Fig. 3 B–F clearly show different mitochondrial structures in each layer

demonstrates two points. First, it shows the effectiveness of the sectioning capability of temporal focusing for activating a single layer within the cell, thereby preventing activation of molecules in other layers. Such extraneous activation in other layers would result in lower axial sectioning and higher background. Second, it shows temporal focusing can be used to activate photoactivatable fluorescent proteins deep inside

the cell and thus allows the collection of super resolution images at multiple axial locations within the sample. This has not been possible thus far with PALM and STORM, because these techniques have been limited to areas within 1 μm of the surface.

Fig. 3G shows the superposition of Fig. 3 B–F with colors coding for the axial position. Although the axial resolution in temporal focusing is significantly lower than the lateral resolution, individual PALM images at 1- μm steps can be combined to create a volume and rendered in three-dimensions. The 3D reconstruction of the images presented in Fig. 3 extends axially over a region of $\approx 5 \mu\text{m}$ and laterally over $\approx 15 \mu\text{m}$. It clearly shows the relative spatial relation of different mitochondrial structures in three dimensions. Although the strength of temporal focusing PALM primary lies in the sectioning capability over large axial regions and the resulting capability for super resolution at depth, the super resolution images from individual layers can also be combined to create a three-dimensional rendering allowing the visualization of relative location of biological structures in a volume (see animation in [Movie S2](#)). The lacking super resolution in the third dimension in this approach can be improved by combining temporal focusing PALM with a recently developed technique which allows super resolution imaging in all three dimensions, but only over an axial length of 0.25 μm . (Shtengel G., Galbraith J.A., Galbraith C.G., Lippincott-Schwartz J., Gillette J.M., Manley S., Sougrat R., Waterman C.M., Kanchanawong P., Davidson M.W., Fetter R.D., Hess H.F., personal communication). This combination would then enable three-dimensional isotropic super resolution imaging in whole cells.

As a second example, we have demonstrated temporal focusing PALM in live *Drosophila* S2 cells expressing membrane targeted Dronpa (Fig. 4A) (Pfeiffer B., Rubin G.M., personal communication). PALM images were taken at six consecutive axial layers each separated by 1 μm ; a representative layer and its close up are shown in Fig. 4D and F. Fig. 4C and D and their respective close ups, Fig. 4E and F, show the comparison between the PALM image of a membrane region and the respective diffraction limited image both taken at the same axial depth. The PALM image in Fig. 4D shows details on the membrane region and some regions closer to the centre of the image (I and II) which are clearly below the resolution of the diffraction-limited image, Fig. 4C. This is more evident in the close up images Fig. 4E and F. As in Fig. 3, the axial position of each PALM image was further used for color coding, and the images were subsequently superimposed, Fig. 4B. This color coded image displays information about the axial structure of the cell membrane, showing a sharp edge of $\approx 2.5 \mu\text{m}$. Areas marked as III and IV that are laterally within 200 nm are axially separated by $\approx 2.5 \mu\text{m}$. The axial topology of the membrane is thus revealed by using temporal focusing PALM.

Outlook. Using temporal focusing to generate PALM images in a volume has several key advantages. First, the optical sectioning characteristics provided by temporal focusing results in a higher signal to noise ratio over a larger axial range than previous techniques. In this sense, the ultimate imaging depth with temporal focusing can be expected to be comparable to a two-photon scanning microscope and is ultimately limited by scattering and aberrations*. Second, by using a slightly modified

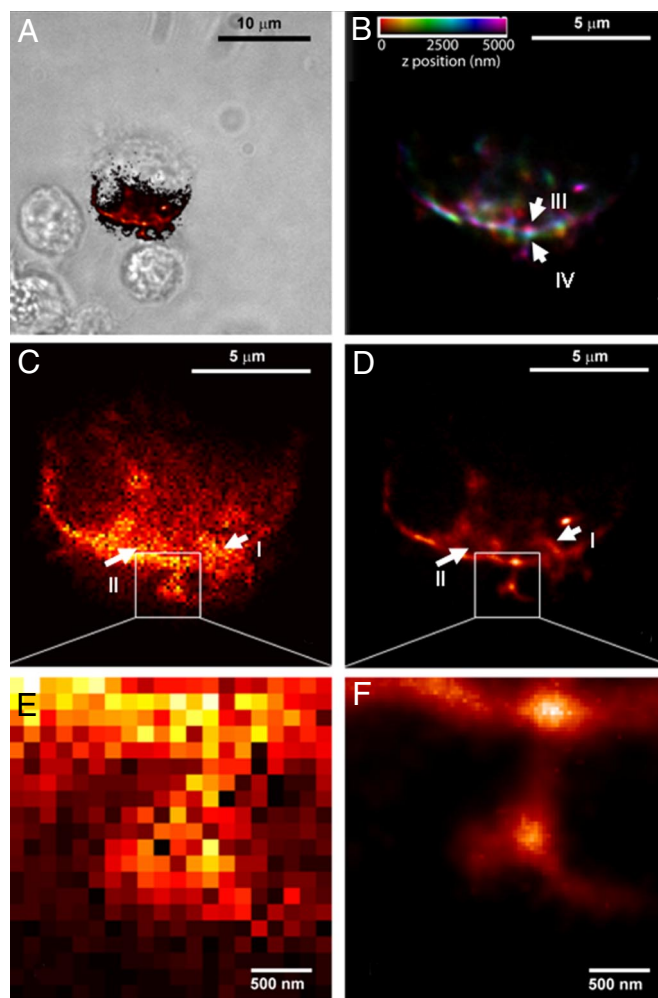


Fig. 4. Multilayer PALM of *Drosophila* S2 cells. (A) Stack of PALM images at six axial layers separated by 1 μm each are taken from membrane labeled *Drosophila* S2 cells. The axial position of each layer is used for color coding and the superimposed images are shown in (B). The color information clearly shows the axial structure of the cell membrane showing a sharp axial edge between III and IV of $\approx 2.5 \mu\text{m}$ over a lateral extension of less than $\approx 200 \text{ nm}$. (C and D) Comparison between PALM and diffraction-limited images for one of the layers. Although the area marked as I is resolved in the PALM image (D), it is clearly below the diffraction limit in (C). The area II in (D) shows a ring type structure that is not resolved in (C). Close-ups (E and F) show protrusions from the membrane. These are individually resolved in (F) and are below the diffraction limit in (E). (A) is a DIC/PALM overlay, showing the S2 cell and the region PALM-imaged in (B–F).

configuration and by using an objective with a higher numerical aperture, the axial resolution of temporal focusing could be improved to $\approx 0.8 \mu\text{m}$. As mentioned earlier, the temporal focusing could then be combined with existing methods for

in each lateral plane. As a result, although in the conventional two-photon microscope, the axial integration over the out-of-focus fluorescent light from each lateral plane is one of the factors limiting the ultimate imaging depth, this is not the case in the temporal focusing configuration. For two-photon absorption, the sum energy of the two photons has to match the optical transition energy. Therefore, the separation of spectral components in the lateral plane guarantees that the axial integration over the out of focus volume does not contribute to a two-photon absorption process. This effect is more pronounced for shorter pulses because in the frequency domain they represent a wider spectral range and therefore in the focusing process, a wider separation of the individual frequency components. However, shorter pulses are more susceptible to dispersion as they propagate through a sample that in turn increases the pulse width. In this regard the suitability of ultra short pulses for imaging in depth and its comparison with the widely used 100-fs pulses calls for a systematic experimental study.

*The ultimate imaging depth in temporal focusing when using ultra short pulses (i.e., $\approx 10 \text{ fs}$) is determined by two competing processes; the spectral width (or pulse duration) and dispersion of the ultra short pulses in the sample. In temporal focusing, different frequency components within the pulse enter the back focal plane of the objective at different locations. Therefore, the only location in the sample where these frequency components overlap and create two-photon excitation is the focal plane. In contrast, in a conventional two-photon microscope, all frequency components are distributed equally

9. Huisken J, Swoger J, Del Bene F, Wittbrodt J, Stelzer EH (2004) Optical sectioning deep inside live embryos by selective plane illumination microscopy. *Science* 305:1007–1009.
10. Willig KI, Rizzoli SO, Westphal V, Jahn R, Hell SW (2006) STED microscopy reveals that synaptotagmin remains clustered after synaptic vesicle exocytosis. *Nature* 440:935–939.
11. Donnert G, et al. (2006) Macromolecular-scale resolution in biological fluorescence microscopy. *PNAS* 103:11440–11445.
12. Hess ST, Girirajan TPK, Mason MD (2006) Ultra-High resolution imaging by fluorescence photoactivation localization microscopy. *Biophys J* 91:4258–4272.
13. Sharonov A, Hochstrasser RM (2006) Wide-field subdiffraction imaging by accumulated binding of diffusing probes. *Proc Natl Acad Sci USA* 103:18911–18916.
14. J. Fölling, et al. (2007) Photochromic rhodamines provide nanoscopy with optical sectioning 13. *Angew Chem Int Ed* 46:6266–6270.
15. Wiedenmann J, Nienhaus GU (2006) Live-cell imaging with EosFP and other photoactivatable marker proteins of the GFP family. *Expert Rev Proteomics* 3:361–374.
16. Oron D, Tal E, Silberberg Y (2005) Scanningless depth-resolved microscopy. (Translated from English) *Optics Express* 13:1468–1476 (in English).
17. Zhu GH, van Howe J, Durst M, Zipfel W, Xu C (2005) Simultaneous spatial and temporal focusing of femtosecond pulses. *Optics Express* 13:2153–2159.
18. Denk W, Strickler JH, Webb WW (1990) Two-photon laser scanning fluorescence microscopy. *Science* 248:73–76.
19. Wiedenmann J, et al. (2004) EosFP, a fluorescent marker protein with UV-inducible green-to-red fluorescence conversion. *Proc Natl Acad Sci USA* 101:15905–15910.
20. Tsutsui H, Karasawa S, Shimizu H, Nukina N, Miywaki A (2005) Semi-rational engineering of a coral fluorescent protein into an efficient highlighter. *EMBO Rep* 6:233–238.
21. Habuchi S, et al. (2005) From The Cover: Reversible single-molecule photoswitching in the GFP-like fluorescent protein Dronpa. *Proc Natl Acad Sci USA* 102:9511–9516.
22. Shannon CE (1949) Communication in the presence of noise. *Proc IRE* 37:10–21.

Supporting Information

Vaziri *et al.* 10.1073/pnas.0810636105

SI Materials and Methods

Depth of Field of the Temporal Focusing. A 10-fs laser pulse has a spectral FWHM of approximately 110 nm. In temporal focusing all spectral components of the laser pulse are colocalized in time and space only in the focal plane (Fig. 1). This fact gives temporal focusing (a wide-field technique) a depth of field comparable to a two-photon scanning microscope. Intuitively, the depth of field in temporal focusing will depend on how “quickly” these spectral components diverge in the plane orthogonal to the direction of propagation as a function of axial distance from the focal plane. Following the beam path backwards from the sample to the back focal plane, this translates into a spatial spread of individual frequency components across the back focal plane of the objective. As a result, the two-photon excitation probability and therefore the depth of field in temporal focusing will depend on the range of the frequency spectrum and its spectral density at the back focal plane. From these heuristic arguments, it becomes clear that the factors determining the depth of field in TF are: the numerical aperture (NA) of the objective, the spectrum of the laser pulses, and how this spectrum is spread across the back focal plane that in turn is determined by the combination of the groove density of the grating and the coupling lens.

The following analytical expression for the two-photon excitation probability (TEP) near the sample focal plane can be found by assuming the paraxial approximation (1),

$$\text{TPE}(z) = \frac{1}{\sqrt{1 + \left(\frac{z}{z_R}\right)^2}}. \quad [1]$$

In equation (Eq. S1), z is the distance from the focal plane and z_R is the Rayleigh range of the laser beam given by (C.V.S., unpublished work)

$$z_R = \frac{\pi \tau^2 c^2 s^2 \cos^2 \theta}{\lambda^3 M^2}, \quad [2]$$

where τ is the laser pulse width, λ the center wavelength of the laser, c the speed of light, s the grating period, M the magnification of the system and θ the incident angle of the laser with respect to the grating.

Given our experimental parameters, we measured a depth of focus of 1.9 μm , slightly above the theoretical limit given by [2]. This difference is most likely due to experimental imperfections and optical aberrations.

The optimal depth of focus for a given set of experimental parameters can be achieved by the following condition (3)

$$\frac{c\tau}{\sin(\theta)} \approx \frac{M\lambda}{2NA}, \quad [3]$$

where c is the speed of light, τ the laser pulse width, M the magnification of the imaging system, λ the centre wavelength of the laser and θ the incident angle of the laser with respect to the grating.

As Oron *et al.* (3) have shown, the depth of field in temporal focusing can be further reduced by placing the grating at an angle with respect to the incident beam. In this way, the incident pulse is scanned across the grating within a few picoseconds, which in turn leads to a line scan of the temporally focused beam across the imaging plane. Using this technique, additional depth of field can be gained by sacrificing the image acquisition speed. However, also in the tilted geometry the limit for the depth of focus corresponds to the case where the instantaneous illuminated area on the grating is imaged by the coupling lens and the objective onto a diffraction limited spot (3).

We experimentally determined the depth of field and the axial sectioning capability of temporal focusing in our setup. The depth of focus was measured by examining the two-photon excitation of colloidal quantum dots. Commercially available quantum dots with an emission peak at 520 nm were mixed with polymethyl methacrylate (PPMA) and spin-coated on a microscope cover glass to create a homogeneous fluorescent layer of approximately 80-nm thickness. This sample was then scanned across the focal region of the temporally focused beam using a piezo electric translation stage. The measured two-photon fluorescence as a function of axial displacement is shown in see supporting information (SI) Fig. S1. The depth of field of the temporal focusing with a FWHM of approximately 1.9 μm was then compared with the case when the grating was replaced by a mirror, that is, removing temporal focusing from the system. It showed a 75-fold increase in the depth of field to approximately 150 μm , which corresponds to a Gaussian beam with a waist size of approximately 15 μm .

Dispersion Compensation. Dispersion compensation was necessary, as the ultra-short pulses traveled through multiple dispersive elements (especially the microscope objective). The pulse width was measured at the specimen plane using a fringe resolved autocorrelator. To get near transform limited pulses at the sample approximately 9,000 fs² of negative group velocity dispersion (GVD), compensation was required, which was achieved by reflecting the pulses multiple times off a pair of chirped mirrors and using fused silica glass wedges for fine tuning. Thereby the original pulse width of approximately 12 fs was restored at the specimen location, which is essential for realizing the highest possible optical sectioning of the system as well as effective two-photon absorption of molecules.

1. Durst ME, Zhu G, Xu C (2008) Simultaneous spatial and temporal focusing in nonlinear microscopy. *Opt Commun* 281:1796–1805.
2. Tal E, Oron D, Silberberg Y (2005) Improved depth resolution in video-rate line-scanning multiphoton microscopy using temporal focusing. *Optics Letters* 30:1686–1688.

3. Oron D, Tal E, Silberberg Y (2005) Scanningless depth-resolved microscopy. *Optics Express* 13:1468–1476.

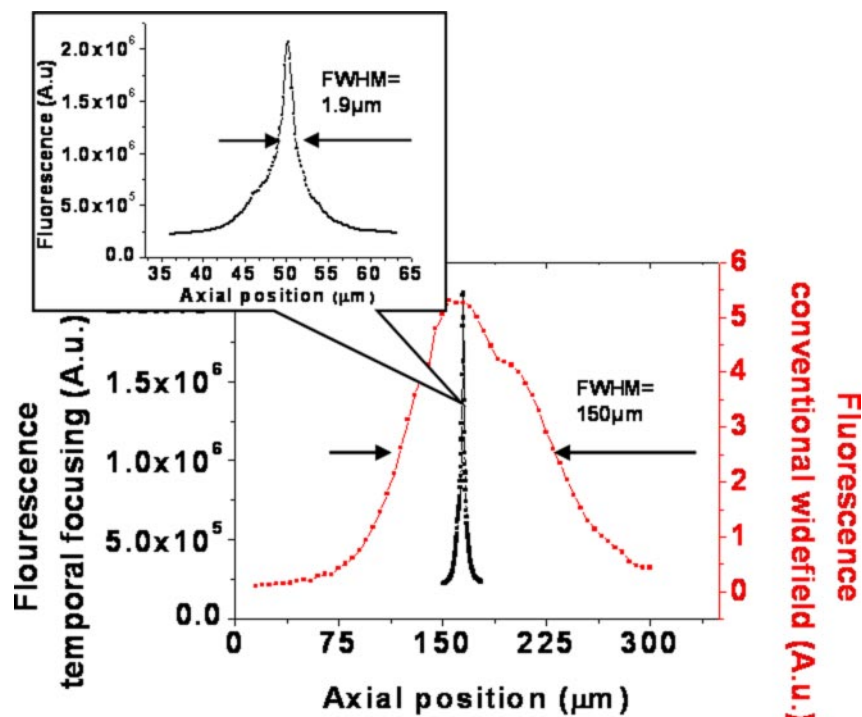
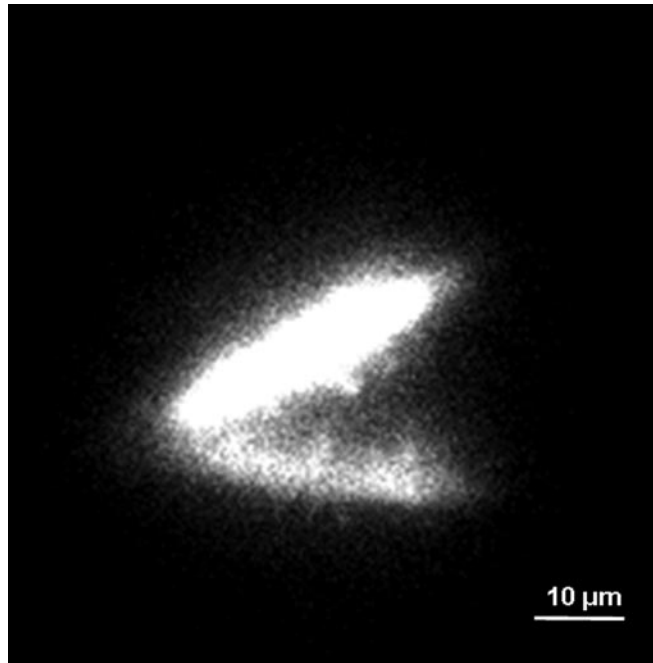
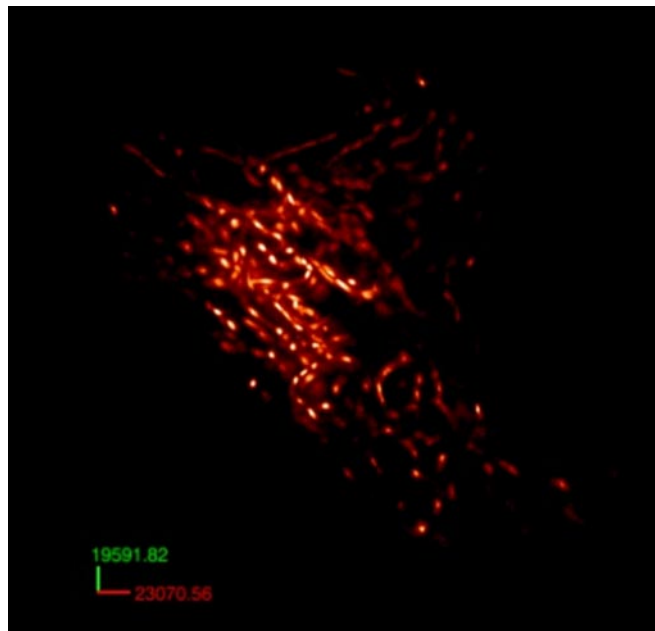


Fig. S1. Comparison depth of field of temporal focusing and conventional wide field. The depth of focus for a temporally focused beam with a spot size of approximately 15 μm is shown. It is approximately 1.9 μm , which is approximately 75 times smaller than for the same spot size without temporal focusing, see SI. The shape of the two-photon excitation curve is proportional to square root of the Lorentzian function and is the result of temporal focusing and the two-photon absorption profile. The slight asymmetry is due to imperfection of the grating.



Movie S1 Optical sectioning of temporal focusing $>100\ \mu\text{m}$ in an acute brain slice. The animation shows a stack of 100 images within an acute hippocampal slice of $400\text{-}\mu\text{m}$ thickness taken at $1\text{-}\mu\text{m}$ steps showing individual dendritic spines microinjected with fluorescent dye. Since the concentration of the dye is much lower than in the spines than in the dendrites the dynamic range of the imaging does not allow proper representation of both structures. Therefore, to be able to visualize the spines clearly, the image of dendrites appears slightly saturated. The animation has the same scale bar as the images shown in Fig. 2B that were taken from this stack. In contrast to Fig. 2B, the relative axial position of the two dendrites is also evident in the animation.

[Movie S1 \(AVI\)](#)



Movie S2. 3D Superr resolution rendering of mitochondrial network. The PALM images shown in Fig. 3 were used to create a volume image of the mitochondrial network over an axial extension of 5 μm . The animation shows different views of this volume in 1° steps over a range of 90° . Although the axial resolution is lower than the lateral resolution the animation clearly allows visualization of subdiffraction structures in 3D. The dynamic scale bar represents the image size in nanometers.

[Movie S2 \(AVI\)](#)